



HAL
open science

Trivalent actinides and lanthanides incorporation in UMo glass-ceramics

Magaly Tribet, Christophe Jegou, Sylvain Peugeot, S Miro, J Delrieu, F.
Doreau

► **To cite this version:**

Magaly Tribet, Christophe Jegou, Sylvain Peugeot, S Miro, J Delrieu, et al.. Trivalent actinides and lanthanides incorporation in UMo glass-ceramics. *Journal of Nuclear Materials*, 2023, 585, <https://doi.org/10.1016/j.jnucmat.2023.154634>. 10.1016/j.jnucmat.2023.154634 . cea-04175125

HAL Id: cea-04175125

<https://cea.hal.science/cea-04175125>

Submitted on 1 Aug 2023

HAL is a multi-disciplinary open access archive for the deposit and dissemination of scientific research documents, whether they are published or not. The documents may come from teaching and research institutions in France or abroad, or from public or private research centers.

L'archive ouverte pluridisciplinaire **HAL**, est destinée au dépôt et à la diffusion de documents scientifiques de niveau recherche, publiés ou non, émanant des établissements d'enseignement et de recherche français ou étrangers, des laboratoires publics ou privés.

Trivalent actinides and lanthanides incorporation and partitioning in UMo glass-ceramics

M. Tribet^{1*}, C. Jégou¹, S. Miro¹, J. Delrieu¹, F. Doreau², S. Peugot¹

¹CEA, DES, ISEC, DPME, Univ Montpellier, Marcoule, France

²CEA, DES, ISEC, DMRC, Univ Montpellier, Marcoule, France

*corresponding author, magaly.tribet@cea.fr

1 Abstract

This article focuses on the Am incorporation and location in the UMo-glass ceramic designed to manage fission product solutions enriched in ²⁴¹Am generated by the reprocessing of UMo spent fuel. This type of glass ceramic contains crystalline phases, which are phosphates, molybdates and zircons, embedded in a durable borosilicate glass matrix.

Two types of UMo-glass ceramics were considered in this study. One type of samples was doped with different amounts of Am and/or Nd to assess the comparative role of Nd versus Am in terms of incorporation, location and microstructure. A second type of sample was doped with ²⁴⁴Cm, in order to specify the behavior of ²⁴⁴Cm compared with that of Nd and Am, with a view to using this short-lived isotope for ageing experiments.

These matrices were characterized by gamma spectrometry and isothermal calorimetry to check the overall homogeneity of Am and Cm, then by Raman spectroscopy, SEM, EPMA and XRD to determine the microstructure and the actinide/Nd distribution in the different phases. The microstructure of the samples was heterogeneous as expected, with the presence of phosphate, molybdate and zircon crystalline phases. A great enrichment of Am, Cm and Nd was observed in the phosphate and molybdate phases compared to the embedding glassy matrix and the zircon crystals. A partition coefficient of around x 6 – 7 for Am and Nd was calculated in these two crystalline phases compared to the mean target doping value. Finally, Nd behaved like trivalent actinides in the UMo matrix and could therefore be considered as a relevant surrogate.

2 Highlights

- UMo waste generated by the reprocessing of UMo spent-fuels from gas-graphite reactors
- UMo glass-ceramic containing phosphate, molybdate and zircon crystalline phases
- In UMo glass-ceramics, crystalline phases are embedded in a glassy matrix
- Am contained in the UMo waste
- Am, Cm and Nd partitioning measured in the UMo glass-ceramic conditioning material
- Nd, an Am/Cm good surrogate with respect to its partitioning into the various phases
- Microstructure of actinide(III) doped UMo-glass ceramics

36 **3 Introduction**

37 Vitrification process has been currently used for decades in many countries to immobilize high-level
38 nuclear waste [1]. The first difficulty in designing a waste package is to find the glass formulation able
39 to chemically incorporate or solubilize the chemical elements contained in the waste. The glass
40 formulations must be compatible with an elaboration by vitrification processes suitable for industrial
41 production in a radioactive environment, and must also produce a material that meets long-term
42 behavior requirements [2, 3]. In some cases, the waste to immobilize could be too complex in terms
43 of chemical composition, or loading rate. In these cases, the waste is not fitted anymore to be easily
44 incorporated in a durable borosilicate homogeneous glass. In such cases, glass-ceramic matrices (GCM)
45 could be an alternative way to confine high amounts of high-level waste [4-8] and could offer a
46 flexibility in the management of waste streams to be vitrified [9, 10].

47 In the specific case of the fission products solutions generated by the reprocessing of UMo spent-fuels,
48 which were used in the past in gas-graphite reactors, molybdenum and phosphorus are the major
49 chemical elements of the waste. However, among the chemical elements of the reprocessing waste,
50 molybdenum is one of the most difficult to incorporate in the borosilicate glasses commonly used [2,
51 11, 12]. In order to meet the expectations in terms of Mo and P incorporation [13-15], it has thus been
52 necessary to develop a specific glass formulation for this wasteform [13, 14, 16], called UMo glass-
53 ceramic. In this UMo matrix, the formation of crystallized phases during the cooling after melting was
54 observed and led to the formation of phosphate, molybdate and zircon phases, embedded in a durable
55 glassy borosilicate matrix [14, 17].

56 It should also be noted that UMo waste solutions were enriched with americium (Am) and that UMo
57 matrices are intended for geological disposal. The behavior of this UMo matrix over geological
58 timescale (thousands of years) has thus to be predicted as best as possible: the question of the Am
59 location in the glass-ceramic is of first importance to assess its long-term behavior because of the quite
60 short half-life of the ²⁴¹Am isotope ($T_{1/2} = 432$ years) regarding to the geological timescale and the
61 subsequent potential alpha decay damage induced in the matrix with time. Such studies, performed
62 on radioactive materials, requires an implementation in hot cell facilities. Such an approach is very
63 expensive and needs at least several years to be implemented. Moreover, only few experimental
64 techniques are available to characterize these radioactive samples. Consequently, it is of first
65 importance to find a good surrogate of americium in such a matrix in order to complete the knowledge
66 about the quality of the resulting matrix versus elaboration conditions, in terms of radionuclides
67 location. Neodymium is a trivalent lanthanide well known to be a good surrogate of trivalent actinides
68 (Am, Cm) in various matrices: glasses, apatite glass ceramics, ceramics [3, 4, 8, 18-22]. Indeed, Nd and
69 (Am, Cm) are very similar concerning their electronic structure with Nd 4f and (Am, Cm) 5f orbitals very
70 localized and their ionic radius. A first study about Nd-doped UMo-glass ceramics shown that Nd
71 preferentially integrated into phosphate and molybdate crystallized phases [14].

72 The present study focuses thus on the trivalent actinides (Am and Cm) distribution in the UMo-glass
73 ceramic in order to check the hypothesis of its possible preferential location and incorporation, based
74 on the Nd non-radioactive simulant. Such an information would help better understanding the Am
75 location in the industrial UMo waste matrix and assessing the use of the ²⁴⁴Cm (as a surrogate of Am)
76 for ageing studies carried out over periods of a few years. Indeed, thanks to its short half-life ($T_{1/2} \sim$
77 18 years), the ²⁴⁴Cm is currently used to mimic the level of alpha decay dose - and the subsequent
78 damage - that the different phases could receive with time, and thus, makes possible to predict the
79 behavior of the real material containing Am over geological periods of time. This methodology is
80 commonly performed on HLW glasses [2, 20] or ceramics [23, 24]. The samples were elaborated in hot
81 cell because of their high radioactivity level. They were then characterized by gamma spectrometry

82 and isothermal calorimetry in order to check for Am and Cm homogeneity and mean amount in the
 83 material, by Raman spectroscopy and XRD to identify the crystallized phases and then by SEM and
 84 EPMA in order to determine the actinide/Nd distribution between the crystallized phases (molybdate,
 85 phosphate and zircon) and the embedding borosilicate glassy phase.

86

87 4 Materials and methods

88 4.1 Glass-ceramics fabrication

89 Four UMo glass-ceramics were fabricated in the DHA-Atalante hot cells facility at CEA-ISEC (Marcoule
 90 research center). Three of them are radioactive materials, respectively doped in term of (LnIII + AnIII
 91 in mol%) with 100 % of Am, 75 % of Cm/25 % of Nd and 50 % of Am/50 % of Nd. The last one is a non-
 92 radioactive material doped with Nd, but elaborated in the hot cell, under the same conditions than the
 93 radioactive samples. The amount of Nd, Am and Cm in the material was chosen to be high enough to
 94 be characterized by calorimetry and EPMA. Furthermore, the ²⁴⁴Cm amount and the ²⁴⁴Cm/Nd ratio
 95 were calculated to meet the expectations in terms of crystalline phases ageing for a couple of years.

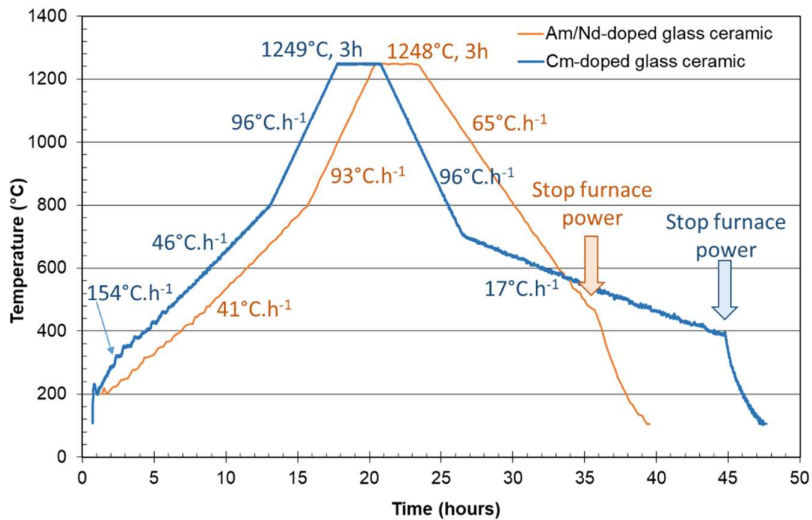
96 The UMo materials were prepared by melting appropriate amounts of oxides, carbonates and nitrates
 97 in Pt/Au-crucibles (15 mm diameter). The curium, the americium and the neodymium elements were
 98 added as their oxide form (CmO₂, AmO₂ and Nd₂O₃ respectively). The AmO₂ powder used had an
 99 isotopic composition of (99.99 ± 0.02) % ²⁴¹Am. The amount of CmO₂ powder incorporated in the Cm-
 100 doped UMo matrix was determined by isothermal calorimetry: the Cm-doped material contained
 101 0.65wt% of ²⁴⁴Cm which corresponded to 0.86wt% of total curium because of the isotopy of the curium
 102 oxide. This sample contains both Cm and Nd, but it is called Cm-doped UMo glass-ceramic hereafter
 103 for simplicity. The expected chemical compositions of these materials are presented in Table 1.

elem. molar%	Si	B	Na	Al	Ca	Mo	P	Zr	Zn	Nd	Am	Cm	Others	O
Cm-UMo	13.71	8.52	6.38	2.96	2.32	1.48	0.93	0.57	1.58	0.025	0	0.075	0.82	60.71
Am-UMo	13.13	8.16	6.14	2.66	2.21	1.82	1.14	1.27	1.52	0	0.152	0	0.61	61.17
Am/Nd-UMo	13.13	8.16	6.14	2.66	2.21	1.82	1.14	1.27	1.52	0.076	0.076	0	0.61	61.17
Nd-UMo	13.13	8.16	6.14	2.66	2.21	1.82	1.14	1.27	1.52	0.152	0	0	0.61	61.17
elem. weight%	Si	B	Na	Al	Ca	Mo	P	Zr	Zn	Nd	Am	Cm	Others	O
Cm-UMo	17.91	4.28	6.82	3.71	4.32	6.60	1.34	2.42	4.80	0.17	0.00	0.86	1.59	45.17
Am-UMo	16.58	3.96	6.35	3.23	3.98	7.85	1.59	5.21	4.47	0.00	1.65	0.00	1.15	44.00
Am/Nd-UMo	16.63	3.97	6.37	3.24	3.99	7.88	1.59	5.23	4.48	0.49	0.83	0.00	1.15	44.14
Nd-UMo	16.69	3.99	6.39	3.25	4.01	7.90	1.60	5.24	4.50	0.99	0.00	0.00	1.15	44.29

104

105 *Table 1: Cm, Am, Am/Nd and Nd-doped UMo glass-ceramic compositions expressed in mol% and in elemental mass% of each*
 106 *element. The global amount of minor elements (Li, Ba, Cr, Mg, Sr, Ni, Fe, Sn, Mn, Cs, Te, Ru, Rh, Y, La, Ce, Pr and U) is referenced*
 107 *as "others".*

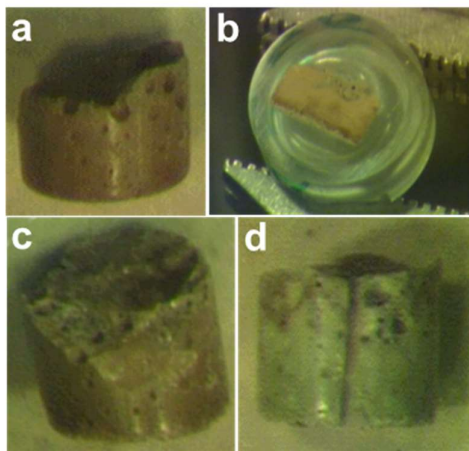
108 Several milliliters of deionized water were added, and the resulting slurry was homogenized by means
 109 of an ultrasonic probe for several minutes. After homogenization, the Pt/Au-crucible was placed in an
 110 alumina container, loaded in a graphite resistor furnace. The furnace atmosphere was then flushed
 111 with Ar for 16h. Melting took place at 1250 °C for 3 hours, under Ar atmosphere. The cooling scenario,
 112 described in Figure 1, was different between the Am, the Am/Nd and the Nd-doped materials
 113 compared to the Cm-doped material, as for this last material preparation, the thermal scenario was
 114 adapted to be as close as possible to that expected at an industrial scale. Pictures of the samples as
 115 fabricated and once removed from the crucible are presented in Figure 2.



116

117 *Figure 1: Thermal history of the Am/Nd and Cm-doped UMo glass-ceramic fabrications.*

118



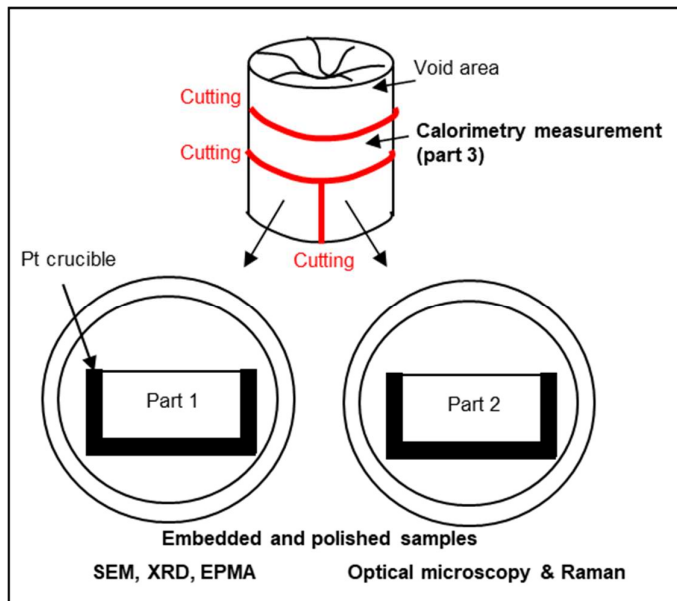
119

120 *Figure 2: Pictures of the Am (a,b), Am/Nd (c) and the Nd-doped (d) UMo glass-ceramics once the crucible removed. The picture*
 121 *(b) corresponds to the Am-doped UMo glass-ceramic embedded and polished sample.*

122

123 The glass-ceramics were then cut and prepared for further solid characterizations. A part (or 2 parts as
 124 for the Cm-doped sample) of the samples were embedded in epoxy resin and then polished to a micron
 125 finish for subsequent structural and microstructural investigations (see Figure 2-b and Figure 3). The
 126 remaining part was used for calorimetry measurements (see Figure 3 as an example).

127



128

129 *Figure 3: Schematic description of the specimen preparation and use concerning the Cm-doped UMo glass-ceramic.*

130

131

132 4.2 Characterization methods

133 As the materials with Am or Cm are highly radioactive, all the characterizations were performed in hot
134 cells, using shielded characterizations devices.

135 4.2.1 Actinide content and homogeneity

136 In order to estimate the homogeneity of the axial Am and Cm distributions, the glass-ceramic rods
137 were analyzed lengthwise by **gamma spectrometry** with a N₂ cooled GeHP EGC15 detector (Camberra,
138 France), on the ²⁴¹Am line (59.5 keV) and ²⁴³Cm lines (228.18 and 277.6 keV). It was performed on the
139 samples as fabricated (Figure 2).

140

141 The ²⁴¹Am and the ²⁴⁴Cm overall contents in the glass-ceramics were determined on samples of around
142 1 - 2 g weight each, by **isothermal calorimetry**. The heat power generated by the glass-ceramic
143 samples was measured in a SETARAM C80D calorimeter (SETARAM France), with a resolution of
144 1.2×10^{-7} W and a detection limit of 2×10^{-6} W. The average of 2 heat power measurements was
145 converted into Am and Cm concentrations by considering a decay heat of 0.11 W.g^{-1} for ²⁴¹Am and
146 2.83 W.g^{-1} for ²⁴⁴Cm and knowing the isotopic composition of the Am and Cm batches used.

147

148 4.2.2 Chemical composition (EPMA) of the different phases

149 The chemical composition of the actinide-doped glass-ceramics was determined by means of a
150 CAMECA SX 50 electron probe micro analyzer (EPMA, Cameca, France) equipped with four X-ray
151 spectrometers and operated under an acceleration voltage of 20 kV and 30 nA stabilized beam.

152 Analytical conditions for secondary phases (crystal, standards, K-L-M lines for each element) are
153 detailed in the Table S1 in Supplementary Data. The standard materials used for Am and Cm

154 quantifications were homogeneous ²⁴¹Am and ²⁴⁴Cm-doped borosilicate glasses fabricated at CEA [25,
155 26], containing respectively 0.85 wt% of AmO₂ and 1.56 wt% of CmO₂. Their Am and Cm contents were
156 previously very well characterized by mixing various characterization methods: isothermal calorimetry,
157 EPMA, and hot acid dissolution of specimens coupled with ICP-AES analyses.

158 The relative uncertainty for Am, Cm and Nd content is of 10%, except in the embedded glass phase,
159 where it is specified. The detection limit (LOD) is of 0.01 at%.

160

161 From the elemental quantitative measurements, a partition coefficient (PC)_i was calculated for i = Nd,
162 Am and Cm by applying the following equation:

$$163 \quad PC_i = \frac{(x_i)_{\text{crystalline phase}}}{(x_i)_{\text{mean target doping value}}} \quad \text{Equation 1}$$

164 Were (x_i)_{crystalline phase} is the atomic value (i.e. quantity in at.%) of Nd, Am or Cm in a given crystalline
165 phase, obtained by EPMA measurements, and (x_i)_{mean target doping value} is the mean target doping value of
166 Nd, Am or Cm, as expressed in Table 1 in elem mol % (i.e. at. %).

167

168 4.2.3 Microstructural and structural characterizations

169 X-ray diffraction patterns were recorded on the Cm-doped UMo glass-ceramic in order to determine
170 the nature of the crystalline phases. The examination was carried out using a Seifert 3000
171 diffractometer (GE Sensing, France) in the Bragg-Brentano geometry (2θ range: 10-95°; step 0.01°;
172 time 15 s/step), equipped with a Cu source (λ = 0.15406 nm) (40 kV, 30 mA). The diffractograms were
173 fitted by using the DIFFRAC^{plus} software and the PDF⁴⁺ database (Bruker, USA).

174

175 Scanning electron micrographs were collected on carbon-coated samples with a JEOL 6300 (JEOL,
176 Japan) scanning electron microscope (SEM, 15 kV).

177

178 The Raman spectra were collected with a Horiba LabRAM HR800 micro-Raman spectrometer with a
179 532 nm excitation laser (green) located outside the hot cell and coupled with optical fibers to an optical
180 microscope with an objective turret (from x1.25 to x100) (Optic Peter, France) implemented in the hot
181 cell. The ×100 objective was used for non-polarized confocal Raman spectroscopy.

182

183

184 5 Results

185 5.1 Actinide content and homogeneity in the glass ceramics

186 The overall ²⁴¹Am and ²⁴⁴Cm contents, obtained by isothermal calorimetry measurements are
187 presented in Table 2 for the Am, Am/Nd and Cm-UMo glass ceramics. Concerning the Cm-UMo glass
188 ceramic sample, this result was in very good agreement with the mean target doping value in ²⁴⁴Cm.
189 Concerning the glass ceramics containing ²⁴¹Am, the ²⁴¹Am content measured by calorimetry in the

190 samples is slightly lower than the mean target doping value, by 3.8% for the Am-UMo sample and by
 191 14.5% for the Am/Nd-UMo sample.

192

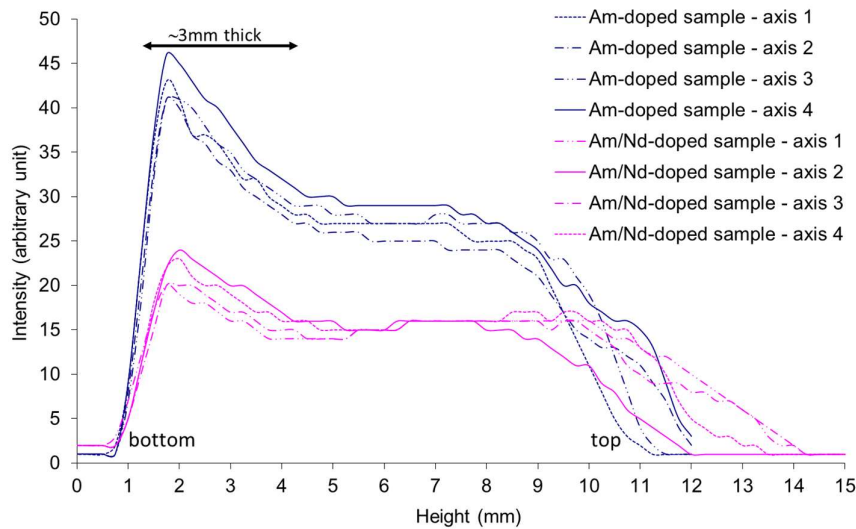
	measured by calorimetry (and compared to expected values)	
content in wt.%	²⁴¹ Am	²⁴⁴ Cm
Am-UMo	1.59 (1.65)	
Am/Nd-UMo	0.71 (0.83)	
Cm-UMo		0.66 (0.65)

193 Table 2: ²⁴¹Am and ²⁴⁴Cm content in the glass ceramics, determined by isothermal calorimetry and expressed in wt.%.
 194 Comparison with the mean targeted doping values, deduced from Table 1 and given between brackets.

195

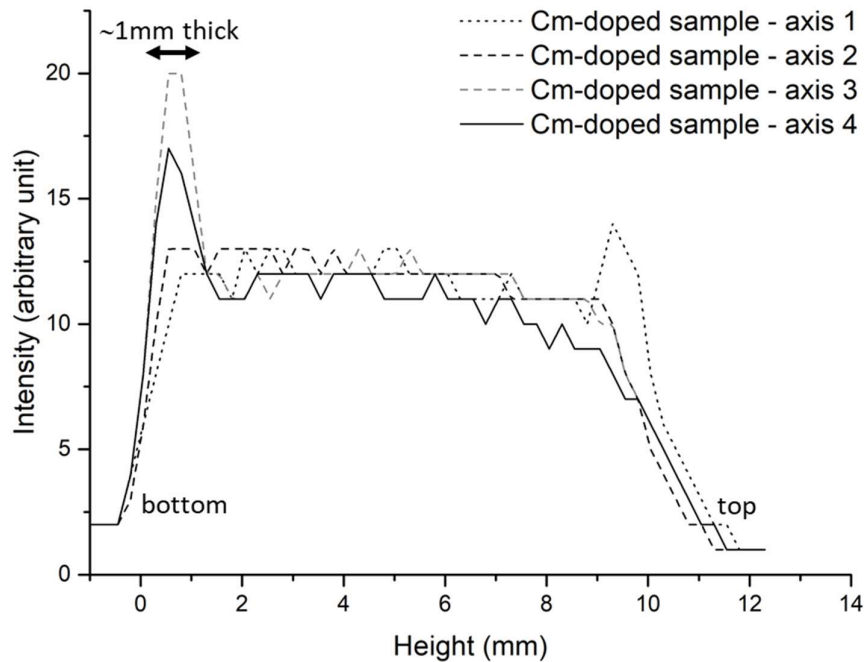
196 Concerning the homogeneity of Am and Cm distributions measured by gamma spectrometry, with the
 197 exception of the bottom enrichment, the major part of the sample lengthwise (i.e. more than 50% of
 198 the length) has a homogeneous Am and Cm distribution, as illustrated in Figure 4 concerning the doped
 199 materials containing ²⁴¹Am and in Figure 5 concerning the ²⁴⁴Cm-doped UMo matrix. This actinide
 200 enrichment of the bottom could be explained by the absence of mechanical stirring during the
 201 elaboration process that could favor a sedimentation of the heavy elements at high temperature. The
 202 relative enrichments observed in the bottom could thus explain the lower ²⁴¹Am content measured by
 203 calorimetry in the middle-part of the Am and Am/Nd-doped samples, compared to the mean target
 204 doping values. This difference in the ²⁴⁴Cm amount was not observed in the case of the ²⁴⁴Cm-UMo
 205 material because the enrichment area of the bottom was localized in a thinner part: 1 mm height
 206 compared (Figure 5) to around 3 mm height for the ²⁴¹Am-doped materials (Figure 4).

207



208

209 Figure 4: Evolution of the ²⁴¹Am gamma peak intensity versus the height of the sample according to 4 longitudinal axis .



210

211 *Figure 5: Evolution of the ²⁴⁴Cm gamma peak intensity versus the height of the sample. Various longitudinal axis (expressed*
 212 *in degree) were explored.*

213 To sum up, except the slight differences in the ²⁴¹Am content and the ²⁴¹Am and ²⁴⁴Cm enrichments
 214 observed at the bottom of the rods (Figure 4 and Figure 5), the samples met expectations in terms of
 215 global Am and Cm mean incorporation in the samples. Moreover, as detailed in Table 2, the mean Am
 216 content in the Am/Nd-doped UMo glass-ceramic was qualitatively half the Am content measured in
 217 the Am-doped UMo glass-ceramic, as expected from Table 1.

218

219 5.2 Microstructure of the glass-ceramics after fabrication

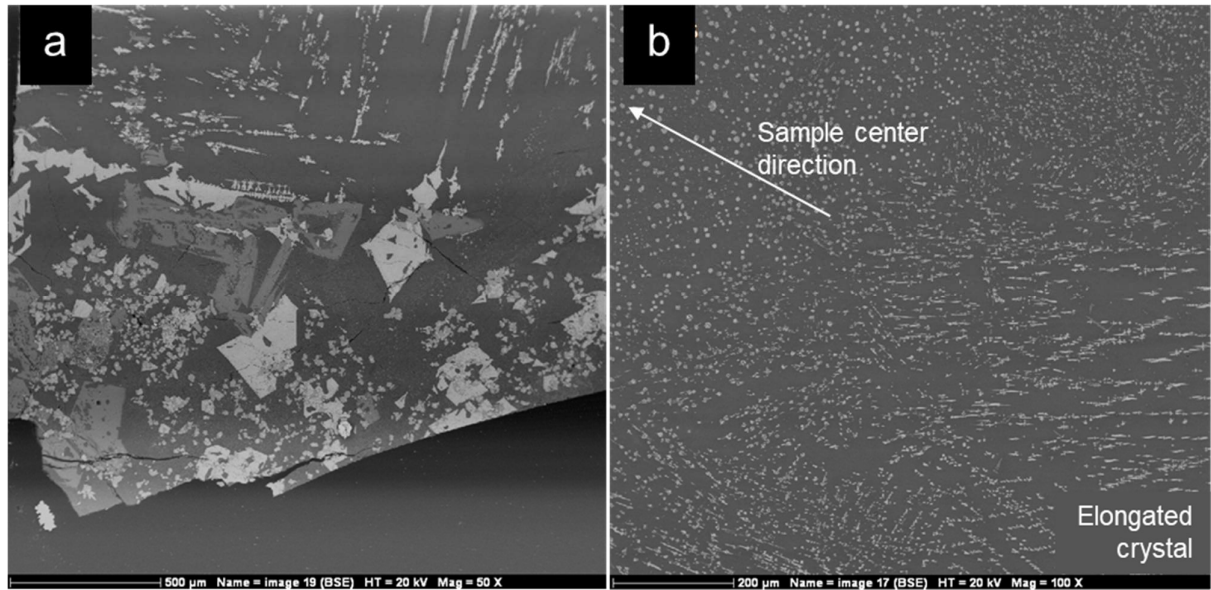
220 The microstructure of the samples were characterized by both optical (Figure S1 in Supplementary
 221 Data) and electronic microscopies (Figure 6 and Figure 7). The different phases observed were
 222 identified by Raman spectroscopy (Figure 7 and Figure 8) and X-ray diffraction patterns (Figure 9). As
 223 similar microstructures were observed on all the samples, the following figures aim to illustrate the
 224 results without systematically presenting pictures for all of them.

225 Bubbles were present in the upper part of the samples (area A on Figure S1) and an important
 226 crystallization was noticed around the bubbles (not observable here, at this scale). At the vertical glass-
 227 ceramic / crucible interfaces, elongated dendritic shaped crystalline phases were observed (Figure 6-b
 228 and are B on Figure S1), which corresponds to the molybdate phase according to Raman spectroscopy
 229 (Figure 7). The microstructure of the center of each sample included small size phases of around 10-
 230 15 μm diameter (top part on Figure 6-b and Figure 7-d; area C on Figure S1). Finally, a sedimentation
 231 zone, containing rectangular base crystals ranging from ten to several hundred microns length, was
 232 observed at the bottom (Figure 6-a and Figure 7-a; area D on Figure S1): these crystalline phases are
 233 very similar to the one observed closed to the bubbles and are composed of the three crystalline
 234 phases molybdate, phosphate and zircon (Figure 7).

235

236 The SEM characterization with backscattered electrons shown the presence of heavy elements in **all**
237 these secondary crystalline phases as they appeared in a lighter greyscale than the borosilicate residual
238 glassy matrix (Figure 6 and Figure 7).

239



240

241 *Figure 6: SEM micrographs (backscattered electrons) of the Am/Nd-doped UMo glass-ceramic sample: (a) the bottom part*
242 *and (b) near the right side. White and light dark phases correspond to crystal phases and the dark grey corresponds to the*
243 *embedding glassy phase.*

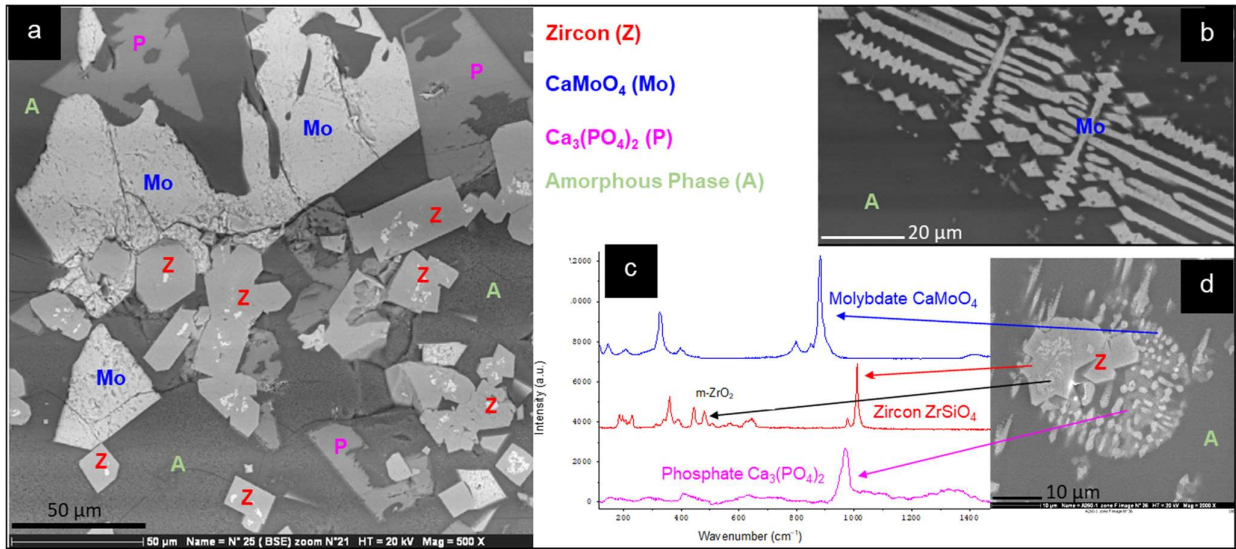
244

245 The different phases were thus analyzed by Raman spectroscopy in confocal mode (Figure 7). Thus,
246 this analysis allowed the determination of three kinds of Raman spectra corresponding to the following
247 phases: calcium molybdate, zircon, calcium phosphate. A fourth Raman spectrum corresponding to
248 the surrounding glassy phase (see Figure S2 in Supplementary Data) was obtained.

249 Raman spectra in agreement with molybdate [27] and phosphate phases [28-30] were observed
250 everywhere in the samples, both in the clusters and in the zone of strong crystallization at the bottom
251 of the glass ceramic samples. The phosphate phase presents **two** different spectra depending on the
252 analyzed area (Figure 8). This can come from local changes in chemical composition and different
253 crystal symmetries. This fact will be develop later, in the Discussion section. In addition, zircon and
254 zirconia crystals ($m\text{-ZrO}_2$ for monoclinic zirconia, with the A_g peak at 476 cm^{-1}) were also identified [31-
255 33] in the zone of strong crystallization at the bottom of the rod and sometimes in large crystallized
256 clusters (Figure 7). The zirconia crystals were very small (<1 micron length) and were included in the
257 zircon phase: in the Figure 7-d, they appear in a lighter greyscale in the zircon crystal.

258 Finally, the SEM characterization coupled with the Raman spectroscopy gave some valuable
259 information on the crystalline phases observed on these samples. The use of Raman spectroscopy
260 made it possible to go a step further in the description of the crystalline phases compared to the
261 previous publication on this UMo material [13, 14, 16].

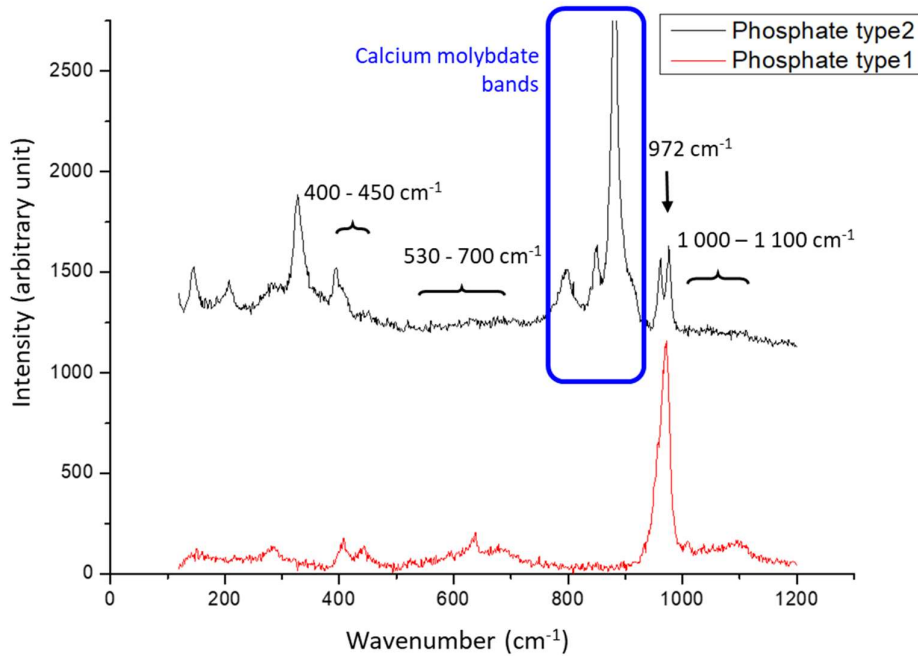
262



263

264 Figure 7: SEM micrographs (backscattered electrons) of the secondary phases and associated Raman spectra (zircon, calcium
 265 molybdate and calcium phosphate). (a) zoom (x 500) of the Figure 6-a) micrograph in the bottom part of the Am/Nd-doped
 266 UMo glass-ceramic, (b) zoom (x 1000) of the same sample in the right side, (c) and (d) are from the center of the Cm-doped
 267 UMo glass-ceramic (x 2000).

268

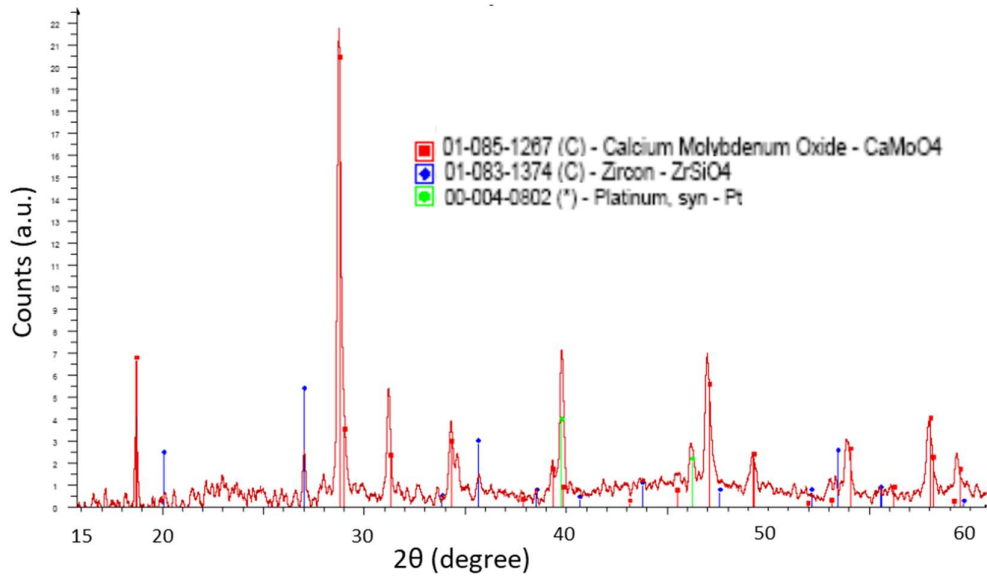


269

270 Figure 8: Example of the two types of Raman spectra found in the phosphate phase in the Cm-doped UMo glass-ceramic.

271

272 The X-ray diffraction patterns of the UMo samples, as illustrated for the Cm-doped UMo sample,
 273 (Figure 9), showed reflections assigned to calcium molybdate and zircon. The platinum crucible signal
 274 was also noticed on the Cm-doped sample as the crucible was not removed on this sample after
 275 fabrication (see Figure 3). No signal from the phosphate phase nor the m-ZrO₂ were observed.



276

277 *Figure 9: Cm-doped UMo glass-ceramic X-ray diffraction patterns. All the reflections were assigned using the PDF4+ database:*
 278 *in red, CaMoO₄; in green zircon crystal and in green platinum from the crucible (as described in Figure 3). No peaks were*
 279 *observed after 60°.*

280

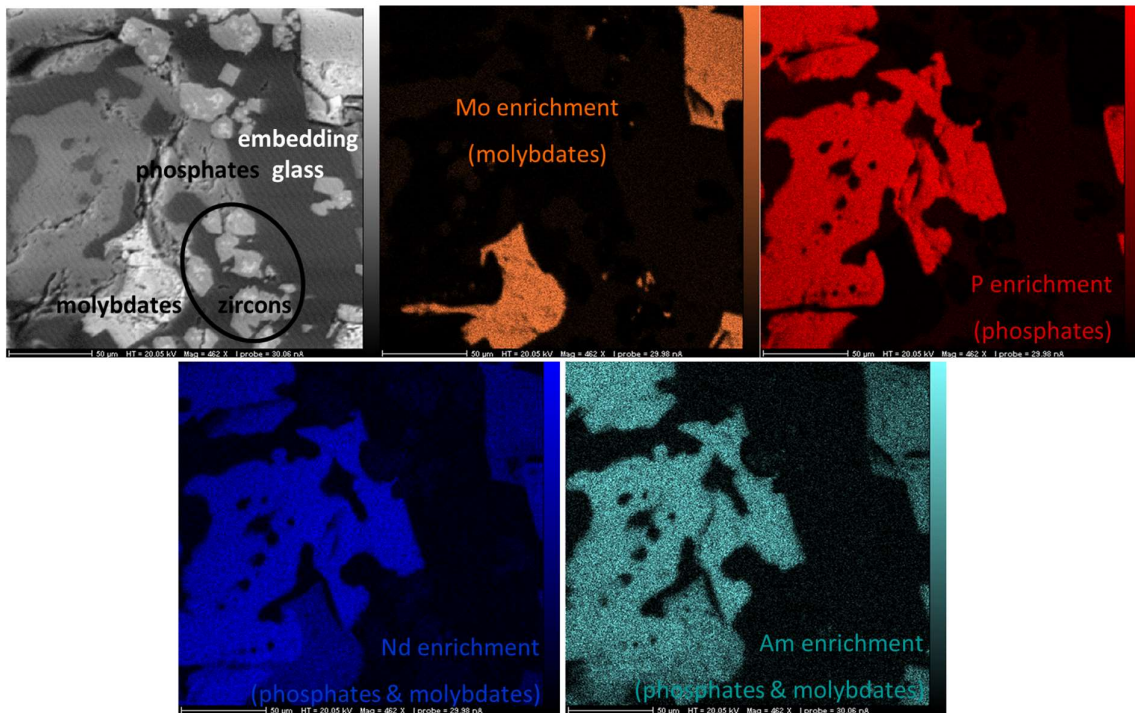
281 5.3 Am, Cm and Nd distribution in the glass-ceramics

282 The relative enrichments in Am, Cm and Nd in the crystallized phases and the embedding glass are
 283 presented qualitatively in the mapping pictures obtained on the Am/Nd-doped matrix (Figure 10) and
 284 from EPMA quantitative measurements (Table 3). A great enrichment in Am, Cm and Nd was observed
 285 in the phosphate and molybdate phases compared to the mean target doping value, the embedding
 286 borosilicate glass and the zircon phase (Table 4). No detectable amount of Am, Nd and Cm was even
 287 evidenced in the zircon phase.

288 In the molybdate phases, 1.2 at.% of Am was measured in the Am-UMo sample and a total of 0.99 at.%
 289 of (Am+Nd) was measured in the Am/Nd-UMo sample (Table 3). In the phosphate phases, 1.1 at.% of
 290 Am was measured in the Am-UMo sample and a total of 1.0 at.% of (Am+Nd) was measured in the
 291 Am/Nd-UMo sample. By taking into account the 10% uncertainty on the EPMA quantitative
 292 measurements of Am and Nd, it can be considered that these concentrations between the Am-UMo
 293 and the Am/Nd-UMo samples were similar, and therefore that similar enrichments were measured in
 294 both phosphate and molybdate phases concerning the Am and Am/Nd-doped UMo glass ceramics.
 295 Moreover, by analyzing the data in the Am/Nd-UMo sample, Am and Nd remained globally equally
 296 distributed in these different phases (0.54/0.45 of Am/Nd in at.% in the molybdate phases and
 297 0.47/0.53 in the phosphate phases), compared to the theoretical relative doping (half Am/half Nd).

298 Concerning the Cm-UMo glass ceramic (Table 3), in both the molybdate and the phosphate phases, Nd
 299 was in slightly lower quantity versus Cm (Cm/Nd ~ 3.5 in the molybdate phase and Cm/Nd ~ 4.3 in the
 300 phosphate phase) than expected from the mean target doping value (Cm/Nd=3, Table 3). Furthermore,
 301 the phosphate phase seemed slightly enriched in both Cm and Nd compared to the molybdate phase.
 302 All these observations could be due to less statistics in the measurements as only 10 quantitative
 303 measurements were performed on each phase of this Cm-doped UMo sample, compared to around
 304 50 quantitative measurements on each phase of the Am-doped samples. Indeed, in the molybdate

305 phase, by taking into account the 10% uncertainty on the EPMA quantitative measurements, the
 306 measured Cm/Nd values, ranging from 2.9 to 4.3 could overlay the mean target doping value of 3.0.
 307



308
 309 *Figure 10: Electronic microprobe mapping of the Am/Nd-doped UMo.*

310

at %		Am-UMo	Am/Nd-UMo	Cm-UMo
mean target doping value	Am	0.152	0.076	
	Nd		0.076	0.025
	Cm			0.075
molybdate	Am	1.2	0.54	
	Nd		0.45	0.15
	Cm			0.65
phosphate	Am	1.1	0.47	
	Nd		0.53	0.25
	Cm			0.88
zircon	Am	< LOD	*	
	Nd		*	*
	Cm			*
embedding glass	Am	0.05 ± 0.03	*	
	Nd		*	0.01 ± 0.01
	Cm			0.06 ± 0.02

311
 312 *Table 3: EPMA quantitative data concerning Am, Nd and Cm atomic concentrations in the different phases of the UMo glass-*
 313 *ceramics. * = not measured. Uncertainties were of 10% when they are not specified.*

314

315

316 6 Discussion

317 This discussion aims to focus first on the UMo-samples microstructure and second on the (Am, Cm)/Nd
318 incorporation and partitioning.

319

320 Regarding the phosphate phase microstructure, two types of Raman spectra were observed as
321 described in Figure 8. These two kinds of Raman spectra showed some similar bands with a main one
322 located around 972 cm^{-1} and other contributions around 400-450, 530-600 and $1000\text{-}1100\text{ cm}^{-1}$. The
323 main peak situated around 972 cm^{-1} corresponds to an orthophosphate compound, with isolated PO_4^{3-}
324 [28]. Moreover, these bands are in agreement with the internal vibration modes of the free PO_4^{3-} [29],
325 observed as follows: $\nu_1 = 938\text{ cm}^{-1}$, $\nu_2 = 420\text{ cm}^{-1}$, $\nu_3 = 1017\text{ cm}^{-1}$ and $\nu_4 = 567\text{ cm}^{-1}$. The ν_1 and ν_3 modes
326 correspond to elongations of the P–O bonds and the ν_2 and ν_4 modes correspond to angular
327 deformation (O–P–O) [30]. All these modes are Raman active. The signatures of these two kinds of
328 Raman spectra could thus correspond either to a monazite-type phase, containing actinides and/or Nd
329 [34, 35], either to a calcium phosphate phase [28, 29, 36-38]. Concerning the type-2 Raman spectrum
330 (in black on Figure 8), a double peak was observed around 950 cm^{-1} . This could correspond to a possible
331 Ca substitution by Na [39, 40] or to an allotropic calcium phosphate (β phase instead of α) [41]. Note
332 that the NaCaPO_4 phase studied by Gbureck et al. has a stoichiometry compatible with the present
333 EPMA results in the UMo matrix, with almost identical contents of Na, Ca, P in the phosphate phase
334 (results presented in the Table T2 in Supplementary Data). The EPMA failed to detect Mg, which rules
335 out the hypothesis of a Merrillite-like phase. In conclusion, it remained difficult to conclude on the
336 exact nature of the type-2 phosphatic phase observed in the UMo matrix: a weak substitution of Ca by
337 Na, a solid solution in the Rhenanite structure with less sodium than calcium or a β -type calcium
338 phosphate are all possible.

339

340 Regarding (Am,Cm)/Nd incorporation in the sample and their partitioning in the different phases (i.e.
341 the crystalline phases and the embedding glassy matrix), the isothermal calorimetry results gave a
342 global view of the samples whereas the EPMA measurements allows to focus on their partitioning in
343 the different phases at the micron scale. As the global Am and Cm incorporation in the samples met
344 expectations, the EPMA results can be compared to the mean target doping value given in Table 1. A
345 partition coefficient can be calculated by applying Equation 1 and is presented in Table 4. Two main
346 results can be highlighted from these EPMA measurements.

347 Firstly, it is obvious that Nd can be considered as a relevant surrogate of both Am and Cm as the
348 Nd/actinide mean target doping values is relatively well preserved in the molybdate and the phosphate
349 phases. This similar behavior was also observed on another glass-ceramic wastefrom having silicate
350 apatite crystals, in which comparison on Nd and Am incorporation was recently studied [4]. Therefore,
351 further studies can thus be performed on such non-radioactive UMo materials, by using Nd instead of
352 trivalent actinides.

353 Secondly, a preferential incorporation of Nd, Am and Cm was clearly observed in the phosphate and
354 the molybdate phases, with a partition coefficient ranging from 6 to 12 (Table 4). The great ability of
355 crystalline phases to incorporate actinides is known in the literature [3, 42]. In these crystalline
356 materials, actinides occupy specific atomic positions in the periodic structure. This allows high loadings
357 of these actinides, but it imposes suitable ionic radius, charge, and bonding constraints in order them
358 to be successfully incorporated in the crystalline structures. Some authors showed the ability of
359 CaMoO_4 to incorporate neodymium or others trivalent rare earth elements [15, 43, 44]. They assumed

360 [15, 43] or observed [44] that this result could be extended to trivalent actinides. Concerning the
 361 phosphate phase, monazite-like structures can incorporate high amount of trivalent actinides [45].
 362 Finally, the greater ability for trivalent actinides or Nd to be incorporated in the crystalline structure
 363 instead of the embedding glass matrix was already observed in quite similar glass ceramics [4]. It is
 364 thus not surprising here to observe their favored incorporation in these molybdate and phosphate
 365 phases compared to the embedded glass matrix.

366

Glass-ceramic	Am -UMo	Am/Nd-UMo		Cm-UMo	
Considered doping element	Am	Am	Nd	Cm	Nd
Molybdate phase	x (7.9 ± 0.8)	x (7.1 ± 0.7)	x (5.9 ± 0.6)	x (8.7 ± 0.9)	x (6.0 ± 0.6)
Phosphate phase	x (7.3 ± 0.8)	x (6.2 ± 0.6)	x (7.0 ± 0.7)	x (11.8 ± 1.2)	x (10.0 ± 1.0)

367 *Table 4 : Partition coefficients of Am, Cm and Nd in the phosphate and the molybdate phases of the studied glass ceramics,*
 368 *calculated from Equation 1.*

369

370 Finally, this preferential partitioning of trivalent actinides in phosphate and molybdate phases
 371 compared to the embedded glass matrix is a crucial result with regard to the ageing of the UMo-matrix.
 372 Indeed, the damage caused by alpha-decay would entirely take place in these two crystalline phases.
 373 Thanks to this work, the level of nuclear dose induced by Am alpha-decay in these crystalline phases
 374 can be calculated versus time and versus the amount of Am incorporated in the UMo matrix, by using
 375 the partition coefficient around x 6 – 7 for Am in these two crystalline phases previously measured
 376 (Table 4).

377

378 7 Conclusion

379 In this paper, we considered four glass-ceramics fabricated in hot cell and containing Nd and/or
 380 trivalent actinides (Am; Cm). This type of glass-ceramic is composed of crystalline phases, which are
 381 phosphates, molybdates and zircons, embedded in a durable borosilicate matrix. The overall ²⁴¹Am and
 382 ²⁴⁴Cm contents in the samples, measured by isothermal calorimetry, were consistent with the expected
 383 global doping rates. Concerning the ²⁴¹Am and ²⁴⁴Cm longitudinal distribution in the cylindrical rods,
 384 except a slight enrichment in the bottoms correlated to a high amount of crystalline phases, the major
 385 part of the sample lengthwise showed a homogeneous Am and Cm distribution. However, the
 386 microstructure of the sample was heterogeneous as expected, with the presence of phosphate,
 387 molybdate and zircon phases embedded in a glassy matrix. Nd behaved like trivalent actinides in these
 388 UMo matrices and can thus be considered as a relevant surrogate of trivalent actinides in terms of
 389 incorporation, location and resulting microstructure in the UMo matrix. In conclusion, the strategy
 390 consisting in using Nd as a surrogate for studies carried out in non-radioactive environments, including
 391 at a full industrial scale [14], is validated by the results presented in the present work.

392 Finally, a higher Am, Cm and Nd partitioning was observed in the phosphate and molybdate phases
 393 compared to the embedding borosilicate glass and the zircon phase. This is identified by a partition
 394 coefficient around x 6 – 7 for Am and Nd in these two crystalline phases compared to the mean target
 395 doping value. To go further, as Am has preferential locations in the UMo matrix, the alpha decay dose
 396 received by these phases could be potentially high enough to suspect changes in their structure and
 397 macroscopic properties [46-48]. Ageing studies by considering the ²⁴⁴Cm-doped UMo matrix would be
 398 of first importance to assess the consequences of such doses on the integrity of the UMo matrix –
 399 mostly on the crystalline phases and their vicinity – versus time.

400

401 8 Acknowledgments

402 The authors would like to thank Orano for its financial support and all the LMPA team for their work
403 performed in the hot cells of DHA unit of ATALANTE facility. They also would like to thank D. Roudil
404 and R. Caraballo, now retired, for their contribution on sample preparation and Raman
405 characterization.

406

407 9 References

- 408 1. IAEA, *Status and Trends in Spent Fuel and Radioactive Waste Management*, ed. N.E.S.N. NW-
409 T-1.14. 2018, Vienna.
- 410 2. Gin, S., et al., *Radionuclides containment in nuclear glasses: an overview*. *Radiochimica Acta*,
411 2017. **105**(11): p. 927-959.
- 412 3. Weber, W.J., et al., *Materials Science of High-Level Nuclear Waste Immobilization*. *Mrs*
413 *Bulletin*, 2009. **34**(1): p. 46-53.
- 414 4. Bardez-Giboire, I., et al., *Americium and trivalent Lanthanides incorporation in high-level*
415 *waste glass-ceramics*. *Journal of Nuclear Materials*, 2017. **492**: p. 231-238.
- 416 5. Caurant, D. and O. Majérus, *Glasses and Glass-Ceramics for Nuclear Waste Immobilization*, in
417 *Encyclopedia of Materials: Technical Ceramics and Glasses*, M. Pomeroy, Editor. 2021,
418 Elsevier: Oxford. p. 762-789.
- 419 6. Donald, I.W., B.L. Metcalfe, and R.N.J. Taylor, *The immobilization of high level radioactive*
420 *wastes using ceramics and glasses*. *Journal of Materials Science*, 1997. **32**(22): p. 5851-5887.
- 421 7. Delaye, J.M., et al., *Molecular dynamics simulation of radiation damage in glasses*. *Journal of*
422 *Non-Crystalline Solids*, 2011. **357**(14): p. 2763-2768.
- 423 8. Miro, S., et al., *Monitoring of alpha-decay radiation damage in a 241Am-doped glass-ceramic*
424 *material*. *Journal of Nuclear Materials*, 2023. **580**: p. 154397.
- 425 9. Jantzen, C.M. and M.I. Ojovan, *On Selection of Matrix (Wasteform) Material for Higher*
426 *Activity Nuclear Waste Immobilization (Review)*. *Russian Journal of Inorganic Chemistry*,
427 2019. **64**(13): p. 1611-1624.
- 428 10. Ojovan, M.I., V.A. Petrov, and S.V. Yudintsev *Glass Crystalline Materials as Advanced Nuclear*
429 *Wasteforms*. *Sustainability*, 2021. **13**, DOI: 10.3390/su13084117.
- 430 11. Caurant, D., et al., *Effect of molybdenum on the structure and on the crystallization of SiO2-*
431 *Na2O-CaO-B2O3 glasses*. *JOURNAL OF THE AMERICAN CERAMIC SOCIETY*, 2007. **90**(3): p.
432 774-783.
- 433 12. Magnin, M., et al., *Effecto of compositional changes on the structure and crystallization*
434 *tendency of a borsilicate glass containing MoO₃*, in *Environmental Issues And Waste*
435 *Management Technologies In The Materials And Nuclear Industries XII*. 2009.
- 436 13. Pinet, O., et al., *Glass matrices for immobilizing nuclear waste containing molybdenum and*
437 *phosphorus*. *JOURNAL OF NUCLEAR MATERIALS*, 2008. **377**(2): p. 307-312.
- 438 14. Pinet, O., et al., *Glass ceramic for the vitrification of high level waste with a high molybdenum*
439 *content*. *JOURNAL OF NUCLEAR MATERIALS*, 2019. **519**: p. 121-127.
- 440 15. Henry, N., et al., *Heat treatments versus microstructure in a molybdenum-rich borosilicate*.
441 *Journal of Non-Crystalline Solids*, 2004. **333**(2): p. 199-205.
- 442 16. Schuller, S., et al., *Phase separation and crystallization of borosilicate glass enriched in MoO₃,*
443 *P2O₅, ZrO₂, CaO*. *Journal of Non-Crystalline Solids*, 2008. **354**(2): p. 296-300.
- 444 17. Vance, E.R., et al., *Leaching behaviour of and Cs disposition in a UMo powellite glass-*
445 *ceramic*. *Journal of Nuclear Materials*, 2014. **448**(1): p. 325-329.

- 446 18. Kidari, A., et al., *Solubility and partitioning of minor-actinides and lanthanides in alumino-*
447 *borosilicate nuclear glass*. Atalante 2012 International Conference on Nuclear Chemistry for
448 Sustainable Fuel Cycles, 2012. **7**: p. 554-558.
- 449 19. Peugeot, S., et al., *Effect of alpha radiation on the leaching behaviour of nuclear glass*. Journal
450 of Nuclear Materials, 2007. **362**(2-3): p. 474-479.
- 451 20. Peugeot, S., J.M. Delaye, and C. Jegou, *Specific outcomes of the research on the radiation*
452 *stability of the French nuclear glass towards alpha decay accumulation*. Journal of Nuclear
453 Materials, 2014. **444**(1-3): p. 76-91.
- 454 21. De Echave, T., et al., *Effect of clayey groundwater on the dissolution rate of SON68 simulated*
455 *nuclear waste glass at 70 degrees C*. Journal of Nuclear Materials, 2018. **503**: p. 279-289.
- 456 22. Tribet, M., et al., *Leaching of a zirconolite ceramic waste-form under proton and He2+*
457 *irradiation*. Radiochimica Acta, 2008. **96**(9-11): p. 619-624.
- 458 23. Mitamura, H., et al., *ALPHA-DECAY DAMAGE EFFECTS IN CURIUM-DOPED TITANATE CERAMIC*
459 *CONTAINING SODIUM-FREE HIGH-LEVEL NUCLEAR WASTE*. JOURNAL OF THE AMERICAN
460 CERAMIC SOCIETY, 1994. **77**(9): p. 2255-2264.
- 461 24. Wiss, T., et al., *Helium release from plutonium and curium-doped zirconolite*. Journal of
462 Nuclear Materials, 2007. **362**(2): p. 431-437.
- 463 25. Peugeot, S., et al., *Irradiation stability of R7T7-type borosilicate glass*. Journal of Nuclear
464 Materials, 2006. **354**(1-3): p. 1-13.
- 465 26. Fillet, S., et al., *Leaching of Actinides from the French LWR Reference Glass*. Material Research
466 Society Symposium Proceedings, 1985. **50**: p. 211–218.
- 467 27. Brinkman, K., et al., *Single phase melt processed powellite (Ba,Ca)MoO4 for the*
468 *immobilization of Mo-rich nuclear waste*. Journal of Alloys and Compounds, 2013. **551**: p.
469 136-142.
- 470 28. Popović, L., D. de Waal, and J.C.A. Boeyens, *Correlation between Raman wavenumbers and*
471 *P=O bond lengths in crystalline inorganic phosphates*. Journal of Raman Spectroscopy, 2005.
472 **36**(1): p. 2-11.
- 473 29. de Aza, P.N., et al., *Vibrational Properties of Calcium Phosphate Compounds. 1. Raman*
474 *Spectrum of β-Tricalcium Phosphate*. Chemistry of Materials, 1997. **9**(4): p. 912-915.
- 475 30. Dekhili, R., et al., *Raman spectra in LiH2PO4 and KLi(H2PO4)2: Mode assignment*. Journal of
476 Raman Spectroscopy, 2019. **50**(3): p. 447-453.
- 477 31. Ji, P., et al., *Direct Observation of Enhanced Raman Scattering on Nano-Sized ZrO2 Substrate:*
478 *Charge-Transfer Contribution*. Frontiers in Chemistry, 2019. **7**.
- 479 32. Atkinson, I., O.C. Mocioiu, and E.M. Anghel, *A study of zircon crystallization, structure, and*
480 *chemical resistance relationships in ZrO2 containing ceramic glazes*. Boletín de la Sociedad
481 Española de Cerámica y Vidrio, 2022. **61**(6).
- 482 33. Kim, B.K. and H.O. Hamaguchi, *Mode assignments of the Raman spectrum of monoclinic*
483 *zirconia by isotopic exchange technique*. PHYSICA STATUS SOLIDI B-BASIC RESEARCH, 1997.
484 **203**(2): p. 557-563.
- 485 34. Bregiroux, D., et al., *Solid-State Synthesis of Monazite-type Compounds Containing*
486 *Tetravalent Elements*. Inorganic Chemistry, 2007. **46**(24): p. 10372-10382.
- 487 35. Silva, E.N., et al., *Vibrational Spectra of Monazite-Type Rare-Earth Orthophosphates*. Optical
488 Materials, 2006. **29**: p. 224-230.
- 489 36. Xie, X., et al., *Natural high-pressure polymorph of merrillite in the shock veins of the Suizhou*
490 *meteorite*. Geochimica et Cosmochimica Acta, 2002. **66**(13): p. 2439-2444.
- 491 37. Zhai, S., et al., *Synthesis and characterization of strontium–calcium phosphate γ-*
492 *Ca3–xSrx(PO4)2 (0≤x≤2)*. Materials Chemistry and Physics, 2010. **120**(2): p. 348-350.
- 493 38. Fix, W., H. Heymann, and R. Heinke, *Subsolidus Relations in the System 2CaO·SiO2-*
494 *3CaO·P2O5*. Journal of the American Ceramic Society, 1969. **52**(6): p. 346-347.
- 495 39. Gbureck, U., et al., *Antimicrobial potency of alkali ion substituted calcium phosphate*
496 *cements*. Biomaterials, 2005. **26**(34): p. 6880-6886.

- 497 40. Quillard, S., et al., *Structural and spectroscopic characterization of a series of potassium-*
498 *and/or sodium-substituted β -tricalcium phosphate*. *Acta Biomaterialia*, 2011. **7**(4): p. 1844-
499 1852.
- 500 41. Jillavenkatesa, A. and R.A. Condrate, *The Infrared and Raman Spectra of β -and α -Tricalcium*
501 *Phosphate ($\text{Ca}_3(\text{PO}_4)_2$)*. *Spectroscopy Letters*, 1998. **31**(8): p. 1619-1634.
- 502 42. Ewing, R.C. and W. Lutze, *High-level nuclear waste immobilization with ceramics*. *Ceramics*
503 *International*, 1991. **17**(5): p. 287-293.
- 504 43. Patil, D.S., et al., *Impact of rare earth ion size on the phase evolution of MoO_3 -containing*
505 *aluminoborosilicate glass-ceramics*. *Journal of Nuclear Materials*, 2018. **510**: p. 539-550.
- 506 44. Bosbach, D., et al., *Trivalent actinide coprecipitation with powellite (CaMoO_4): Secondary*
507 *solid solution formation during HLW borosilicate-glass dissolution*. *Radiochimica Acta*, 2004.
508 **92**(9-11): p. 639-643.
- 509 45. Holliday, K.S., et al., *Site-selective time resolved laser fluorescence spectroscopy of Eu and Cm*
510 *doped LaPO_4* . 2012. **100**(3): p. 189-195.
- 511 46. Meldrum, A., et al., *Radiation damage in zircon and monazite*. *Geochimica et Cosmochimica*
512 *Acta*, 1998. **62**(14): p. 2509-2520.
- 513 47. Wang, X., et al., *Irradiated rare-earth-doped powellite single crystal probed by confocal*
514 *Raman mapping and transmission electron microscopy*. *JOURNAL OF RAMAN*
515 *SPECTROSCOPY*, 2014. **45**(5): p. 383-391.
- 516 48. Patel, K.B., et al., *Discovery of a maximum damage structure for Xe-irradiated borosilicate*
517 *glass ceramics containing powellite*. *JOURNAL OF NUCLEAR MATERIALS*, 2018. **510**: p. 229-
518 242.
- 519